Journal of Ceramic Processing Research. Vol. 27, No. 1, pp. 10~23 (2026)
(Received 26 July 2025, Received in revised form 11 November 2025, Accepted 21 November 2025)
https://doi.org/10.36410/jcpr.2026.27.1.10

J O U R N A L O F
Ceramic Processing Research

Scale-up synthesis of Nano-TiC powder with controllable particle size via salt-assisted combustion method

Faqi Zhan*, Yinyan Du, Hua Zhang, Min Zhu, Yuehong Zheng and Peiqing La*
State Key Laboratory of Advanced Processing and Recycling of Nonferrous Metals, School of Materials Science and Engineering, Lanzhou University of Technology, Lanzhou 730050, China

Ultra-high-temperature materials demonstrate excellent performance, with high-melting-point carbides like titanium carbide (TiC) widely used across industries. With advancing technology, demands for material performance are increasing. Although nano-scale carbides offer advantages, conventional preparation methods face significant challenges. In this study, nano-TiC powder was synthesized using combustion synthesis in the TiO_2-C-Mg system with NaCl as a diluent. This approach effectively mitigates excessive grain growth caused by high combustion temperatures, enabling large-scale production of high-purity nano-TiC. NaCl addition significantly reduces TiC particle size. When NaCl content reaches 100 wt.%, the average particle size decreases from 178 nm to 74 nm, with a specific surface area of 15.203 m^2/g. Particle refinement results from NaCl's dual effects during formation and growth stages. NaCl lowers adiabatic temperature via endothermic phase transformation and creates a liquid-phase environment that enhances diffusion and undercooling, promoting nucleation while suppressing grain growth. This study offers technical guidance for scalable production of nano-TiC with controlled particle size.

Keywords: Salt-assisted combustion, TiC nanopowders, Controllable particle size, Formation mechanism.

Introduction

Ultra-high temperature ceramics (UHTCs) are a class of ceramic materials that exhibit stable performance under extremely high-temperature conditions, typically exceeding 3000 °C. Representative materials include ZrB_2, HfC, and TiC. Among these materials, titanium carbide (TiC) stands out as a representative transition metal carbide, exhibiting a high melting point (3160 °C), high hardness (28.5-32 GPa), excellent elastic modulus, good electrical conductivity, low density, and superior corrosion resistance [1]. Owing to its exceptional physical and chemical properties, TiC has found widespread application not only in the aerospace industry, but also in cutting tools, aerospace thermal protection systems, nuclear engineering, and electronic devices, among various other technological fields [2-5].

Driven by advancements in science and technology as well as improvements in industrial production capabilities, the manufacturing sector has imposed increasingly stringent demands on the particle size, performance, and production scale of TiC. Notably, the particle size, purity, and morphology of TiC exert a significant influence on its functional properties. Submicron or nano-sized powders exhibit distinctive properties, including the small size effect, quantum size effect, and surface effect. These characteristics enable them to be readily dispersed within a matrix, thereby significantly enhancing the performance of composite materials and leading to their widespread application across various fields [6-8]. Nevertheless, the current state of nanopowders development still falls short of meeting industrial requirements: not only in terms of precise control over particle size and purity, but also due to challenges such as high production costs, complex manufacturing processes, and the difficulty of achieving large-scale production [9, 10]. Therefore, the development and application of sub-micron and nano-scale powders are attracting growing scientific and industrial interest. It is anticipated that future technological advancements will enable further size reduction into the nanoscale regime, enhanced purity with reduced impurity content, and improved functional properties. The particle size, purity, and microstructural characteristics of these powders significantly influence their overall performance. Jam et al. fabricated TiC particles with average particle sizes of 1.67 μm and 1.35 μm, respectively, and conducted a systematic investigation into the comprehensive mechanical properties of the corresponding sintered bodies. The results demonstrated that for an average TiC grain size of 1.67 μm, the sintered body exhibited a hardness of 86.4 ± 1 HRA and a flexural strength of 739 ± 24 MPa. When the average grain size was reduced to 1.35 μm, the material achieved optimal comprehensive mechanical performance, with the hardness increasing to

*Corresponding author:
Tel : +86 15209310025
Fax: +86 15209310025
E-mail: zhanfaqi@lut.edu.cn (Faqi Zhan);
pqla@lut.edu.cn (Peiqing La)

89.4 ± 2 HRA and the flexural strength reaching 724 ± 27 MPa. Qiu et al. [11] synthesized TiC powder with a particle size of 607 nm and carried out a preliminary investigation into its sintering behavior. The results demonstrated that TiC ceramics sintered at 2000 °C under a pressure of 40 MPa for a holding duration of 2 h exhibited hardness and fracture toughness values of 15.92 GPa and 3.22 $MPa \cdot m^{1/2}$, respectively. Ko et al. [12] synthesized TiC particles with a nominal size of 100 nm and systematically investigated their effect on the mechanical properties of TiC/Fe_3Al composites. The results demonstrated that the flexural strength of the metal ceramic containing 50 vol.% and 70 vol.% TiC both exceeded 1700 MPa.

Currently, the primary synthesis methods for TiC include carbothermal reduction [13], the sol-gel process [14], mechanical alloying [15], and combustion synthesis [16], among others. Hu et al. [17] employed the carbothermal reduction method to synthesize TiC powders using starch and graphite as carbon sources, respectively. The results indicated that when starch was utilized as the carbon source, the TiC powder synthesized at 1550 °C consisted of spherical particles, ball-like particles (with an average size of approximately 100 to 200 nm), and whiskers (with diameters ranging from 50 to 200 nm). In contrast, when graphite was used as the carbon source, the TiC powder synthesized at 1600 °C exhibited a particle size distribution ranging from 200 to 400 nm, although significant agglomeration or cohesion among the particles was observed. Jia et al. [18] successfully synthesized TiC nanocrystals with particle sizes ranging from 20 to 50 nm via mechanical alloying, employing titanium and various carbon sources. However, this method poses potential contamination risks during the synthesis of TiC nanoparticles and may result in issues such as inhomogeneous particle size distribution, high energy consumption, limited reproducibility, and complicated post-treatment procedures. Therefore, further improvements are required through the synergistic optimization of multiple process parameters. Fahmi et al. [19] synthesized TiC nano-powders with particle sizes ranging from 20 to 100 nm using the sol-gel method. However, this approach is relatively complex and requires precise control over critical stages, including hydrolysis, polycondensation, and drying. It also carries a high risk of introducing impurity phases (e.g., TiO_2), and achieving consistent particle size control remains challenging.

Compared with other preparation methods, combustion synthesis offers several advantages, including a straightforward process, the absence of a requirement for complex equipment, high yield, and the capability for large-scale production. Additionally, the synthesized materials exhibit relatively high purity, and this method has been extensively applied in the field of powder metallurgy [20-22]. Ghazanfari et al. [23] synthesized sub-micron TiC particles via combustion synthesis at 1100 °C (with a heating rate of 500 °C/min). The average particle size of the resulting TiC ranged from 150 nm ± 30 nm to 600 nm ± 50 nm. Zhu et al. [24] synthesized spherical TiC within the Ni-Ti-C system through combustion synthesis and systematically investigated its formation mechanism. The experimental results demonstrate that during the heating process in a vacuum induction melting furnace up to 1200 °C, increasing the heating rate from 5 °C/min to 80 °C/min leads to an increase in the size range of TiC particles from below 1 μm to 2-5 μm. However, when the heating rate is increased from 10 °C/min to 80 °C/min, further elevation of the heating rate exerts a negligible effect on the particle size of TiC. During the combustion synthesis process, the release of a substantial amount of heat leads to a significant rise in system temperature, which promotes the growth of product particles and hinders the synthesis of nano-scale TiC powder. Therefore, addressing the issue of excessively high combustion temperatures is of critical importance for the large-scale production of nanostructured materials. In our preliminary work, we successfully achieved the large-scale synthesis of nano-crystalline zirconium diboride (ZrB_2) powder via a salt-assisted combustion synthesis method, employing NaCl and a NaCl-KCl mixture as diluents. By incorporating molten salt diluents, nano-crystalline ZrB_2 powder with an average particle size of approximately 105 nm and a purity of 99.24% was obtained [25]. Furthermore, studies have demonstrated that nano-SiC can be synthesized using the salt-assisted combustion synthesis method with NaCl as the diluent. It has been observed that increasing the NaCl content leads to a gradual reduction in the particle size of the synthesized SiC powder, with the average size decreasing from 155 nm to 28 nm [26]. Therefore, whether the addition of molten salt diluents yields similar effects and trends in the large-scale synthesis of nano-TiC remains a subject for further investigation.

In this study, the salt-assisted combustion synthesis method was employed within the TiO_2-C-Mg system, utilizing NaCl as a diluent to modulate the thermodynamic and kinetic processes of the reaction, thereby enabling the large-scale synthesis of high-purity nano-TiC powder. The effects of varying diluent contents on the particle size and purity of TiC were systematically investigated, and the role of NaCl in controlling TiC particle growth was elucidated, providing a solid theoretical foundation and technical support for the scalable production of nano-TiC powder.

Experimental

Experimental Materials

Nano-sized TiC was successfully synthesized on a large scale through combustion synthesis. To minimize the impact of raw materials on the properties of the resulting powder, titanium dioxide (TiO_2) and carbon

Table 1. Experimental Materials and Specifications.

Ingredients	Purity (wt.%)	Impurities	Specifications
TiO_2	>99.95	O, Zr, Al	10~20 nm
C	>99.95	O, Na, Ca	30 nm
Mg	>99.5	Cl, S, O	325 mesh
NaCl	AR	Mg, K, Fe, SO_4^{2-}	<200 mesh

black were both selected as nano-sized precursors. Detailed specifications of the raw materials are provided in Table 1.

Sample Preparation

The large-scale synthesis process of nano-TiC follows the methodology established in our previous studies on SiC and ZrB_2 [25, 26], with the sole modification being the substitution of TiO_2 for the original Ti source. All other raw materials and processing conditions remain unchanged. During the synthesis of TiC powder, varying amounts of NaCl (0~110 wt.%) were introduced, and the resulting products were designated as TiC0, TiC30, TiC70, TiC100, and TiC110, respectively.

Characterization Methods

The phase compositions of the samples before and after washing were analyzed using a D/MAX-2400 X-ray diffractometer (XRD). The instrument was operated with a Cu Kα radiation source at a voltage of 40 kV and a current of 40 mA, with a scanning range of 20° to 80° and an X-ray wavelength (λ) of 0.154 nm. XRD analysis enabled the determination of phase composition and structural transformation characteristics, providing insights into the microcrystalline size and lattice strain. The grain size and lattice strain of the powder were estimated based on the full width at half maximum (FWHM) of the diffraction peaks in the XRD pattern. Using the Debye-Scherrer equation (Eq. 1), the average particle size of the combustion-synthesized powder was calculated [27].

$$D = \frac{k\lambda}{\beta cos\theta} \tag{1}$$

In the formula, D denotes the grain size, λ represents the wavelength of the X-ray source, θ refers to the diffraction angle, k is assigned a value of 0.89, and β indicates the full width at half maximum (FWHM) of the diffraction peak, expressed in radians (rad). Furthermore, the chemical composition of the final synthesized sample was verified using a Genesis-XM2 energy-dispersive X-ray spectrometer (EDS), with an operating voltage of 15 kV and a beam current of 10 μA. The presence of free carbon in the product was qualitatively analyzed by means of a Lab RAM HR Evolution micro-laser Raman spectrometer. In addition, the chemical and electronic states of surface elements were quantitatively characterized using a Shimadzu AXIS SUPRA X-ray photoelectron spectrometer (XPS).

The micro-morphology of the prepared powder was examined using a JSM-6700 field emission scanning electron microscope (FESEM), with an operating voltage of 3-5 kV and a beam current of 5-7 μA. The particle size and microstructural features of the samples were further investigated via a JEM-2010 field emission transmission electron microscope (TEM). The particle size distribution was statistically analyzed using Image-Pro software. Additionally, the specific surface area of the synthesized products was measured employing a JM-BK200C specific surface area and pore size analyzer (BET), and the results were evaluated based on Eq. (2):

$$D_{BET} = 6 / \rho S_{BET} \tag{2}$$

In the equation, D_{BET} denotes the equivalent average diameter in micrometers (μm), ρ represents the theoretical density of the carbide phase, and S_{BET} refers to the specific surface area measured by the BET method, expressed in square meters per gram (m^2/g).

Results and Discussion

Thermodynamic calculation of system

Thermodynamic analysis of the reaction system serves as a fundamental basis for investigating the combustion synthesis process. It enables a thorough theoretical examination of the thermodynamic parameters and product composition, thereby offering essential theoretical insights and data support for understanding the product formation mechanisms in various reaction systems [28]. Gibbs free energy (ΔG_T) serves as a critical thermodynamic parameter for assessing the spontaneity of a chemical reaction. A reaction can proceed spontaneously in the direction indicated by the chemical equation only when ΔG_T is less than zero. The standard Gibbs free energy of the reaction ΔG_T^θ is calculated based on Eq. (3) and (4), where ΔH_{298}^θ represents the standard molar enthalpy of formation at 298 K, ΔS_T denotes the entropy change at temperature T, and T refers to the reaction temperature in Kelvin.

$$\Delta G_T^\theta = \Delta H_{298}^\theta + T\Delta S_T \tag{3}$$

$$\Delta S_T = \sum (n_i \Delta S_{i,T})_{product} + \sum (n_i \Delta S_{i,T})_{reactant} \tag{4}$$

In this study, the TiO_2–C–Mg system was employed for the combustion synthesis process. The reaction mechanism comprises two sequential steps: the first involves the reduction of TiO_2 by Mg, and the second entails the reaction of the resulting titanium with carbon to form the final TiC product. The specific reaction equations corresponding to the synthesis of TiC are Eq. (5) and (6).

Table 2. The standard ΔG_T^θ change expression for the reaction.

Reaction	ΔG_T^θ (J·mol^{-1})	Temperature range (K)
$TiO_2(s)+2Mg=Ti(s)+2MgO(s)$	-263157 + 30.2T	298~922
	-276435 + 51.6T	922~1363
	-514289 + 228.5T	1363~2250
$Ti(s)+C(s)=TiC(s)$	-185805 + 11.1T	298~3000

$$TiO_2 + 2Mg = Ti + 2MgO \quad (5)$$

$$Ti + C = TiC \quad (6)$$

The thermodynamic data for the TiO_2-C-Mg system were obtained from the "Handbook of Thermodynamic Diagrams: Inorganic compounds and elements" [29]. Using Eq. (3) and (4), the relationship between the standard ΔG_T^θ of the system's reaction and temperature was calculated, as presented in Table 2.

The relationship between the ΔG_T^θ of the aforementioned reaction and temperature is presented in Fig. 1 The ΔG_T^θ values for reactions (5) and (6) are both negative, indicating that these reactions are thermodynamically spontaneous. Within the TiO_2-C-Mg system, reaction (5) is the most favorable to occur during the initial stage when the temperature is below 1500 K, yielding relatively stable products. Provided that an adequate amount of reducing agent is present, complete reduction of all oxides can be achieved. From a thermodynamic perspective, the reduction of TiO_2 by Mg tends to proceed spontaneously in the forward direction when the temperature is below the equilibrium temperature of 2250 °C (ΔG_T^θ=0). In the second reaction step (6), the reduced titanium reacts with carbon to form TiC. The corresponding Gibbs free energy (ΔG_T^θ) increases with rising temperature; however, it remains negative throughout the experimental temperature range, thereby ensuring the spontaneity of this reaction stage. Based on the variation trend of ΔG_T^θ in the second-stage reaction, it can be concluded that the reaction maintains a negative ΔG_T^θ value across the entire experimental temperature range, indicating that the process is thermodynamically feasible within the TiO_2-C-Mg system.

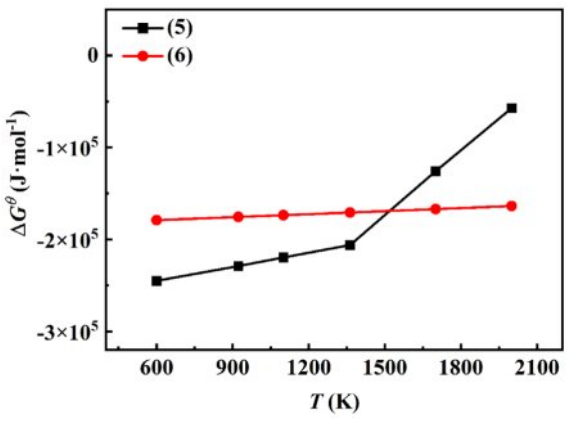

Fig. 1. The ΔG^θ-T relationship diagram of the reaction.

The combustion synthesis process is characterized by a highly exothermic reaction, with the entire process typically completing within a very short time frame (a few seconds). A central focus in the study of self-propagating high-temperature synthesis reactions is whether the reaction can sustain and propagate autonomously once initiated [30, 31]. Research indicates that the combustion synthesis reaction can proceed in a self-sustained manner only when the adiabatic temperature (T_{ad}) is ≥ 1800 K. When T_{ad} is < 1800 K, external heating methods (such as preheating or the use of chemical furnaces) are required to sustain the reaction under normal conditions. Based on thermodynamic data obtained from the "Handbook of Thermodynamic Diagrams: Inorganic Compounds and Elements" [29] and employing Eq. (7), the adiabatic temperature of the system was calculated:

$$-\Delta H_{298}^\theta = \int_{298}^{T_m} \Delta C_{p,m} dT + \Delta H_m + \int_{T_m}^{T_{ad}} \Delta C_{p,m} dT \quad (7)$$

In the formula, ΔH_{298}^θ (kJ·mol^{-1}) represents the standard formation enthalpy of the product at 298 K, $\Delta C_{p,m}$ (J·K^{-1}) is the heat capacity of the product, T_m (K) is the melting point of the product, and ΔH_m (J·kg^{-1}) is the melting heat of the product. $C_{p,m}$ can be approximately calculated using the following formula (8):

$$C_{p,m} = a + b\times10^{-3}T + c\times10^{5}T^{-2} + d\times10^{-6}T^{2} \quad (8)$$

Upon the addition of NaCl to the TiO_2-C-Mg system, the calculated adiabatic temperature is presented in Fig. 2. During the combustion synthesis of TiC under experimental conditions, the adiabatic temperature of the system decreases progressively with increasing NaCl content. The reduction reaction is accompanied by the release of a significant amount of thermal energy. However, given that NaCl possesses a relatively low melting point (1074 K) and boiling point (1735 K), a portion of the generated heat is absorbed by NaCl to facilitate its phase transitions, thereby reducing the overall adiabatic temperature of the system. Fig. 3 presents the differential scanning calorimetry (DSC) curves of the two samples. The results indicate that the addition of the diluent NaCl lowers the overall onset temperature of the SHS reaction; furthermore, the incorporation of NaCl introduces a new endothermic peak, thereby contributing to a reduction in the system's undercooling.

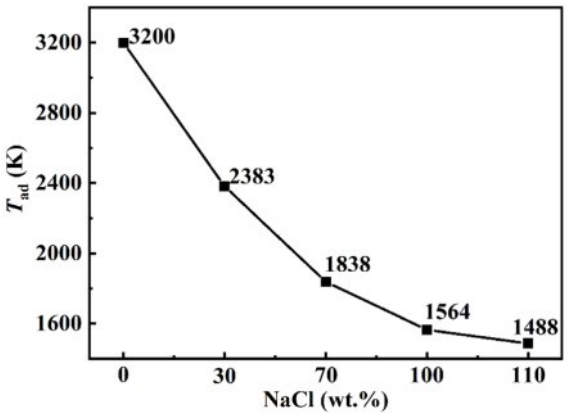

Fig. 2. The correlation between the T_{ad} of the reaction system and the amount of NaCl.

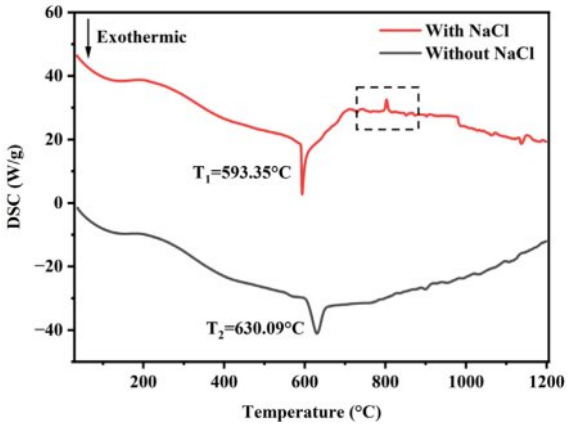

Fig. 3. The DSC curves for the two samples.

Through calculation of the adiabatic temperature of the TiO_2-C-Mg system, it was determined that the system is still capable of sustaining a spontaneous reaction even when the theoretical adiabatic temperature is as low as 1500 K. The analysis of this phenomenon can be attributed to the following factors: (1) Prior to the initiation of the combustion synthesis reaction, under an argon atmosphere of 2.0 MPa, the system must be preheated to approximately 250 °C using external equipment in order to ignite the ignition agent and initiate the self-propagating reaction. As a result, the system has already reached the temperature threshold necessary to sustain the self-propagating reaction when T_{ad} < 1800 K; (2) Achieving a perfectly adiabatic condition in practical reaction systems is challenging. In addition to the influence of preheating temperature, parameters such as pressure and phase transitions of the reactants can also affect the reaction temperature; (3) The ultra-fine particle size of the reactants significantly increases the interfacial contact area, thereby facilitating the reaction at relatively low temperatures. Experimental findings demonstrate that the diluent NaCl effectively absorbs the heat generated during the combustion process, thereby reducing the local reaction temperature and subsequently lowering the overall adiabatic temperature of the system.

Phase composition of TiC powder

The crystallographic phases of the synthesized products under varying NaCl content conditions were characterized using XRD. Fig. 4 presents the XRD patterns of TiC powder before and after washing. Prior to washing, in the absence of NaCl addition, the main phases identified were TiC and MgO. With increasing NaCl content, distinct diffraction peaks corresponding to NaCl emerged, and their intensity increased markedly, as illustrated in Fig. 4a, indicating incomplete volatilization of NaCl during the reaction process. When the addition amount of sodium chloride reached 110%, residual TiO_2 reactants and unreacted magnesium reductants were detected, but no characteristic diffraction peaks of TiC were observed. These results indicate that the synthesis of TiC did not proceed completely under the given experimental conditions. The low melting and boiling points of the molten salt may lead to localized temperature reductions, which can hinder the full progression of the reduction reaction. To remove impurity

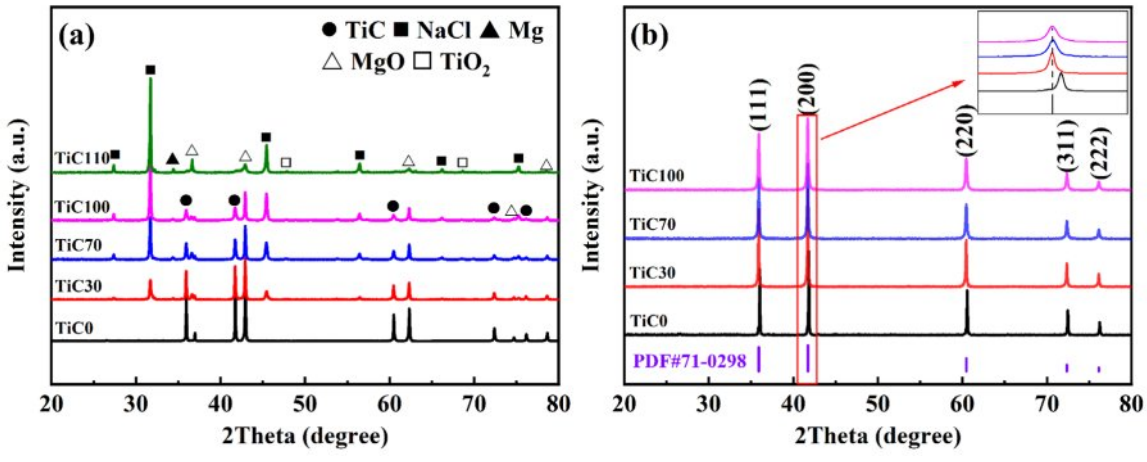

Fig. 4. XRD patterns of TiC powders: (a) before and (b) after washing.

phases, the synthesized product was first subjected to mechanical crushing, followed by repeated washing with hot deionized water at approximately 80 °C under vigorous stirring to ensure complete removal of NaCl. Subsequently, the powder was treated with 0.1 M dilute hydrochloric acid to dissolve and eliminate the MgO by-product, after which it was washed repeatedly with deionized water until the filtrate reached a neutral pH. Finally, the resulting powder was dried in a vacuum oven at 80 °C for 12 h to fully remove residual moisture. As shown in Fig. 4b, all diffraction peaks detected after washing were attributed to the TiC phase. The five major diffraction peaks corresponded to the (111), (200), (220), (311), and (222) crystallographic planes of the standard TiC phase (PDF#71-0298), confirming the high phase purity (>99%) of the synthesized TiC. Furthermore, no additional impurity phases were observed in Fig. 4b, indicating that the acid and water washing procedures effectively removed all by-products, resulting in a single-phase. Fig. 4b inset presents a magnified view of the (200) crystal plane of TiC, which exhibits relatively high diffraction peak intensity. It is evident that with increasing NaCl content, the diffraction peaks shift to lower angles and their intensity decreases. This suggests a gradual increase in the lattice constant of TiC. The variation in the lattice constant can be attributed to the nanoscale grain size and the non-stoichiometric composition of the synthesized carbide. In TiC, the lattice parameter is known to increase with higher carbon content. Moreover, the broadening of the diffraction peak with increasing NaCl content indicates a reduction in the particle size of the product. The grain size corresponding to the (200) crystal plane was calculated using Eq. (1), and the results are summarized in Table 3. As shown, the particle size of the TiC powder decreases with increasing NaCl addition, with the theoretical average grain size reaching as low as 75 nm. These findings demonstrate that the addition of molten salt diluent does not compromise the purity of the final product and, instead, serves as an effective means of controlling grain size.

Table 4 summarizes the mass percentages of individual elements in TiC synthesized with varying amounts of NaCl. The product is primarily composed of three elements: Ti, C, and O. Notably, the oxygen content increases with increasing NaCl addition. XRD analysis confirms the absence of detectable oxide phases,

Table 3. Calculated grain sizes of TiC synthesized based on the (200) diffraction plane.

NaCl (wt.%)	2Theta (°)	Peak FWHM	Grain size (nm)
0	41.83	0.092	180.80
30	41.70	0.125	149.97
70	41.72	0.189	98.12
100	41.73	0.242	75.75

Table 4. The proportion of elemental content in TiC synthesized with different amounts of NaCl.

NaCl (wt.%)	C		Ti		O	
	wt.%	at.%	wt.%	at.%	wt.%	at.%
0	16.9	42.9	80.8	52.4	2.3	4.7
30	18.2	45.7	78.7	49.4	3.1	4.9
70	23.6	53.0	73.0	41.3	3.4	5.7
100	34.9	65.2	60.7	28.7	4.4	6.1

suggesting that the elevated oxygen levels are attributable to enhanced surface oxidation resulting from the progressive refinement of the particles. Furthermore, a corresponding increase in the carbon content is observed with higher NaCl concentrations. As shown in Table 4, the combined mass percentages of Ti and C in all samples exceed 95%, regardless of the diluent amount used. These results demonstrate that the salt-assisted combustion synthesis method enables effective control over particle size while maintaining a high degree of powder purity.

To investigate the distribution of free carbon in the synthesized TiC, Raman spectroscopy was performed on samples prepared under varying NaCl content conditions, with results presented in Fig. 5. The Raman spectra reveal the presence of graphite characteristic peaks (G band) at 1600 cm^{-1} and disorder-induced peaks (D band) at 1350 cm^{-1}, indicating the existence of free carbon within the TiC powder. This is likely attributed to the graphite carbon source, which possesses a high fixed carbon content and relatively low chemical reactivity, leading to minor carbon residue after the reaction. As the NaCl content increases, the intensity of the carbon-related peaks rises significantly, suggesting a corresponding increase in free carbon content. This observation aligns with the EDS elemental analysis results, which also show an increase in the C content. With the reduction in particle size, the specific surface area increases, resulting

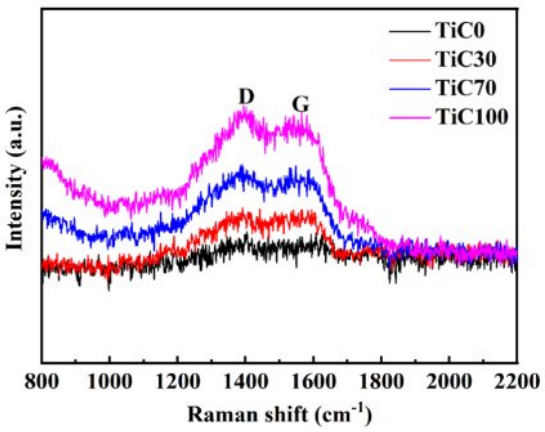

Fig. 5. Raman spectra of TiC synthesized with different amounts of NaCl.

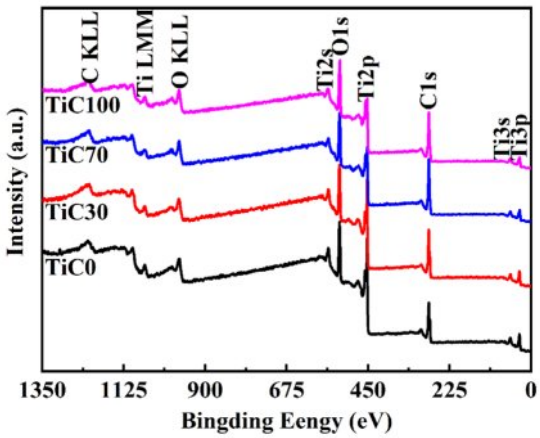

Fig. 6. XPS spectra of TiC synthesized with different amounts of NaCl.

Table 5. XPS atomic ratios of TiC synthesized with different amounts of NaCl.

NaCl (wt.%)	C (at.%)	Ti (at.%)	O (at.%)
0	47.67	40.76	11.57
30	51.88	33.94	14.18
70	52.66	28.51	18.83
100	55.41	24.52	20.07

in greater surface adsorption of carbon. Moreover, the ultrafine nanostructure of the synthesized TiC powder further contributes to the broadening of the main Raman peaks.

Fig. 6 presents the XPS full spectrum of nano-TiC

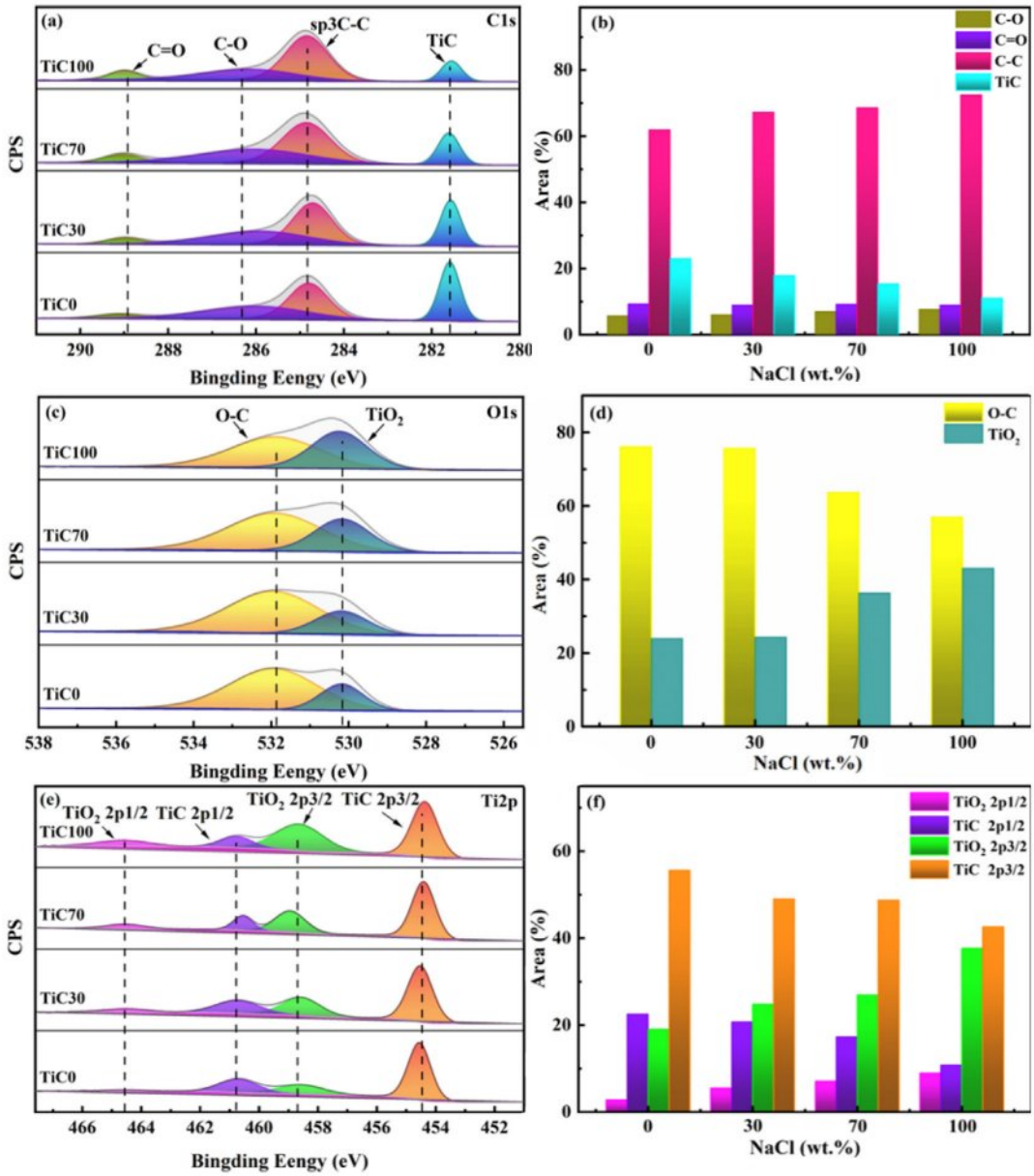

Fig. 7. XPS spectra and chemical state proportions of TiC synthesized with different amounts of NaCl: (a, b) C1s; (c, d) O1s; (e, f) Ti 2p.

Table 6. Particle size indicators for TiC synthesized with different amounts of NaCl.

NaCl (wt.%)	D10 (nm)	D50 (nm)	D98 (nm)	Average particle size (nm)
0	114	169	276	178
30	92	143	225	145
70	59	89	149	96
100	47	75	120	74

Note: D10, D50, and D98 represent the particle size values at which the cumulative particle size distribution of the sample reaches 10%, 50%, and 98%, respectively.

synthesized in a molten salt environment, illustrating the chemical bonding states on the surface of the powder particles. The TiC surface is primarily composed of three elements: Ti, C, and O. The atomic ratios of these elements are summarized in Table 5. Quantitative surface analysis reveals that as the salt content in the system decreases, the composition of the synthesized TiC approaches the ideal stoichiometric ratio. In addition to Ti and C, a small amount of O is also detected on the particle surface, with its content showing a positive correlation with the amount of NaCl added. This observation is consistent with the results of other phase characterization technique.

Fig. 7 presents the high-resolution XPS spectra of C 1s, O 1s, and Ti 2p in TiC, along with the relative proportions of their respective chemical states. The energy scale of the XPS spectra was calibrated using the C 1s peak (281.6 eV) of TiC as a reference. As shown in Fig. 7a, the peaks at binding energies of 281.6 eV, 284.8 eV, 286.4 eV, and 288.9 eV are attributed to Ti-C, C-C, C-O, and C=O bonds, respectively. According to Fig. 7b, the surface carbon content increases gradually with increasing NaCl content. This carbon primarily originates from the bonded carbon within the carbide structure and a small amount of residual free carbon. The observed increase in carbon content is mainly due to the accumulation of unreacted free carbon. Moreover, the increased ratios of C-O and C=O peaks indicate a certain degree of surface oxidation. In the O 1s spectrum shown in Fig. 7c, the peak at 530.2 eV is typically assigned to the O-Ti bond, while the peak at 531.8 eV corresponds to the O-C bond. The features of the O 1s spectrum are consistent with the presence of chemically adsorbed oxides such as CO. No additional impurity oxide peaks were detected. The Ti 2p spectrum in Fig. 7e consists of two spin-orbit doublets: Ti 2p3/2 and Ti 2p1/2. Peaks at

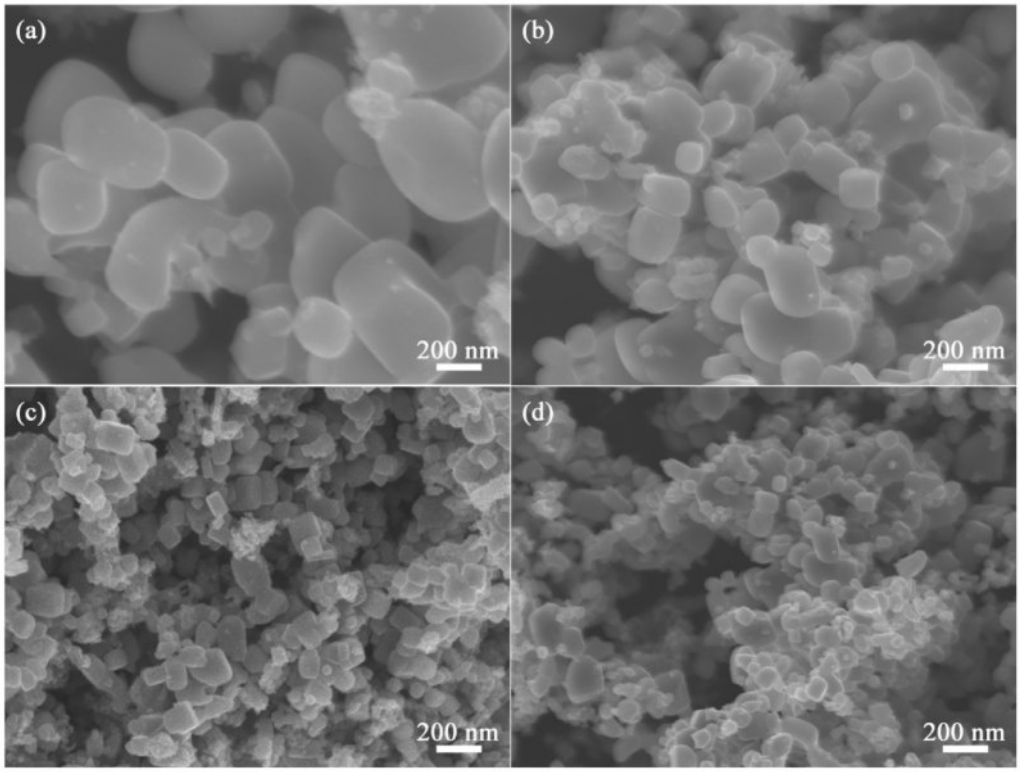

Fig. 8. SEM images of TiC synthesized with different amounts of NaCl: (a) TiC0; (b) TiC30; (c) TiC70; (d) TiC100.

454.5 eV and 460.8 eV are associated with Ti-C bonding, whereas those at 458.6 eV and 464.5 eV are indicative of TiO_2. Quantitative analysis of the Ti 2p orbitals reveals that the relative content of TiO_2 increases with higher NaCl content, suggesting the occurrence of oxygen substitution on the surface of the TiC sample. Based on the results of EDS and Raman spectroscopy analyses, it can be concluded that in the molten salt environment, an increase in NaCl content leads to a decrease in thermal conductivity, resulting in a higher concentration of free carbon on the particle surface. Additionally, the reduction in particle size and the corresponding increase in specific surface area further promote surface oxidation reactions.

Particle size and microstructure of TiC nanopowder

Fig. 8 presents the SEM results of nano-TiC synthesized with varying amounts of NaCl. The TiC synthesized via the magnesium thermal reduction combustion method exhibits a well-defined crystalline structure and excellent dispersion, with no significant interparticle agglomeration observed. All samples display a cubic morphology, and the particle size of the TiC powder decreases with increasing molten salt content in the synthesis system. In the absence of NaCl, the TiC particles are relatively coarse and exhibit an uneven particle size distribution. Potential causes for this observation include: (1) non-uniform mixing of raw materials, leading to local variations in stoichiometric ratios within the reaction zone; and (2) excessively high combustion temperatures, which may result in abnormal grain growth.

With increasing NaCl content, the particle size distribution becomes progressively more uniform. As illustrated in Fig. 8d, the synthesized TiC particles exhibit high crystallinity and a fine particle size, with an average diameter of approximately 70 nm. However, mild agglomeration is observed among some of the smaller particles. This phenomenon can be attributed to the strong interparticle forces and the high specific surface area inherent to nanoparticles, which promote self-aggregation. The addition of NaCl as a diluent reduces the system's adiabatic temperature, thereby facilitating the formation of smaller TiC nanoparticles and effectively mitigating the issue of non-uniform particle size distribution.

Fig. 9 presents the TEM images of TiC powders synthesized with varying amounts of NaCl. In the absence of NaCl addition, the synthesized TiC particles exhibit a relatively large size and an inhomogeneous

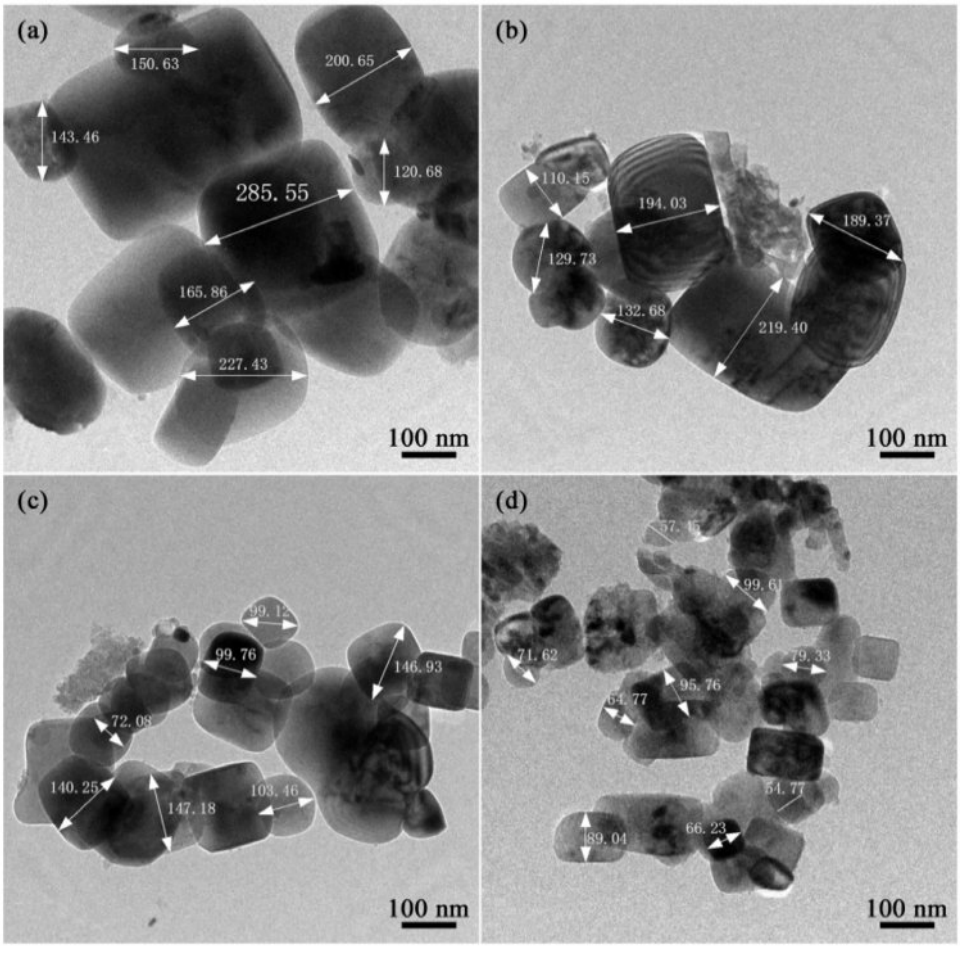

Fig. 9. TEM images of TiC synthesized with different amounts of NaCl: (a) TiC0; (b) TiC30; (c) TiC70; (d) TiC100.

particle size distribution, as illustrated in Fig. 9a. Upon the introduction of the molten salt diluent, a significant reduction in particle size is observed, with the grain size decreasing from over 300 nm to as small as approximately 30 nm (Fig. 9b-d). Most particles display a cubic morphology, while smaller particles tend to adopt a near-spherical shape. When the NaCl content is increased to 100 wt.%, the particle size distribution becomes more uniform; however, slight agglomeration is still observed among the finer particles, which is consistent with the SEM analysis. The results indicate that molten salt NaCl, acting as a diluent, absorbs heat during the synthesis process and effectively suppresses grain growth. Compared to the case without diluent addition, the appropriate incorporation of NaCl enables the synthesis of TiC powders with finer and more uniform particle sizes.

Fig. 10 presents the representative high-resolution transmission electron microscopy (HRTEM) image of the synthesized nano-TiC powder along with its corresponding selected area electron diffraction (SAED) pattern. As illustrated in Fig. 10a, the diffraction rings observed in the SAED pattern, from the innermost to the outermost, correspond to the (111), (200), (220),

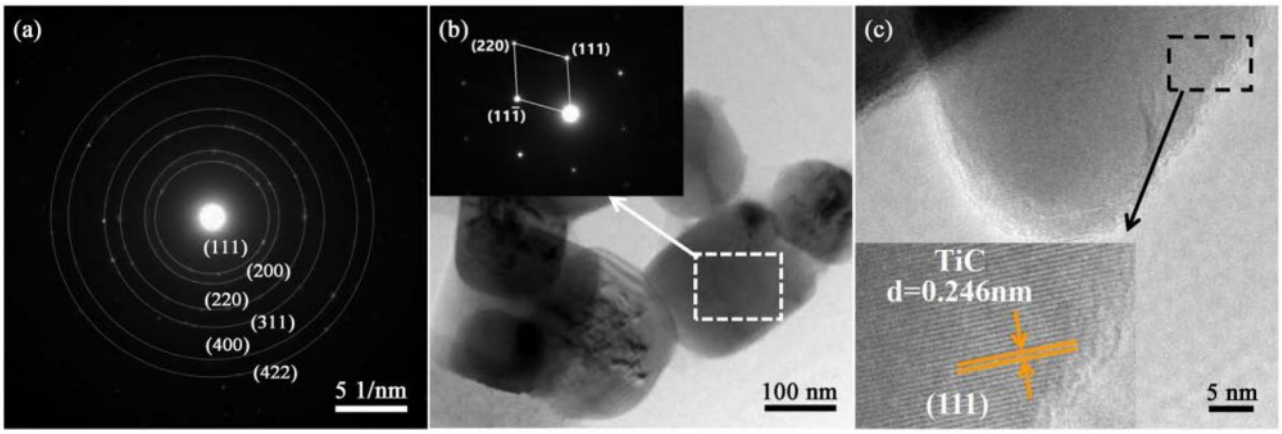

Fig. 10. HRTEM and SAED images of TiC synthesized with different amounts of NaCl: (a), (b) SAED image of TiC30; (c) HRTEM image of TiC100.

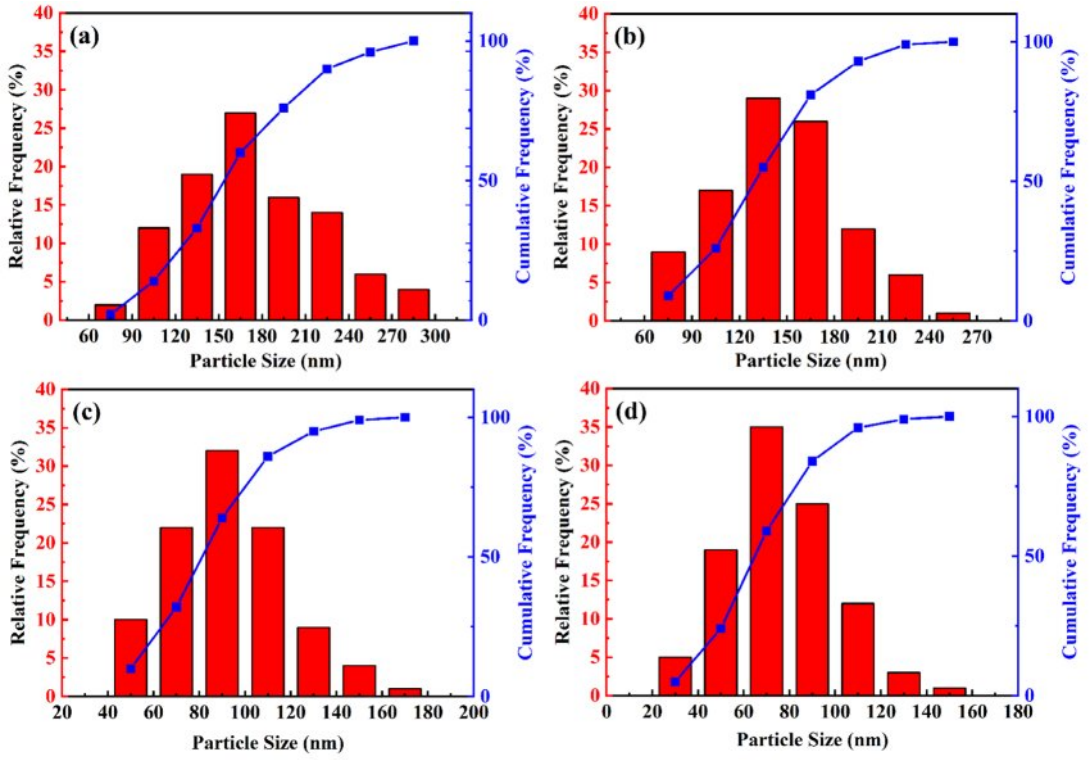

Fig. 11. Particle size distribution diagram of TiC synthesized with different amounts of NaCl: (a) TiC0; (b) TiC30; (c) TiC70; (d) TiC100.

(311), (400), and (422) crystallographic planes of face-centered cubic TiC. These diffraction features exhibit clear polycrystalline characteristics, confirming that the synthesized TiC nanoparticles possess a high degree of crystallinity and excellent dispersion. In the low-magnification bright-field TEM image (Fig. 10b), the particle surfaces appear clean and morphologically flat. The corresponding SAED pattern displays distinct diffraction spots, further supporting the presence of single-crystal domains within the TiC nanostructures. HRTEM analysis provides more direct evidence of the crystalline nature of TiC, revealing continuous and well-defined lattice fringes, as shown in Fig. 10c. These lattice fringes indicate a highly ordered atomic arrangement within the nanoparticles. The measured lattice spacing is 0.246 nm, which closely matches the (111) interplanar spacing of standard TiC (d = 0.249 nm, PDF#71-0298), thereby further confirming the accuracy of the crystal structure.

To investigate the influence of molten salt diluents on the particle size of synthesized TiC powders, TEM images were systematically measured and statistically analyzed to determine the particle size distribution of each sample group. The resulting size distributions are presented in Fig. 11. As indicated by the particle size parameters listed in Table 6, in the absence of NaCl addition, the TiC particle size ranges from 60 to 300 nm, with a significant variation between the smallest and largest particles. When the NaCl content is increased to 70 wt.%, the particle size predominantly falls within the range of 60 to 120 nm, and the median diameter (D50) decreases to approximately 89 nm. Compared with TiC70 powder, TiC100 powder exhibits a smaller particle size, with a median diameter of 75 nm and a minimum size reaching approximately 30 nm. The presence of some larger particles may be attributed to nanoparticle agglomeration during the synthesis process, which increases the proportion of larger particles and affects the overall size distribution. Experimental results demonstrate that as the molten salt NaCl content increases from 0 wt.% to 100 wt.%, the particle size distribution of TiC powder becomes progressively narrower and more uniform. The average particle size decreases from 178 nm to 74 nm, with the finest particles measuring below 30 nm.

Table 7 summarizes the raw materials, preparation methods, and particle size distributions of TiC powder products reported in previous studies. A comparative analysis of the raw materials, preparation methods, and particle size characteristics of the TiC powder synthesized in this study with the data presented in Table 7 indicates that existing methods exhibit notable limitations. For example, high-temperature and prolonged reaction conditions (e.g., No. 10) tend to result in grain coarsening

Table 7. A comparative analysis of the TiC powder prepared in previous studies.

No.	Raw materials	Process conditions	Particle size (nm)	Ref.#
1	325 mesh Ti powder, 30-45 nm Acetylene black;	Disproportionation reaction method in molten salt: 850 °C, 2 h; Dry at 120 °C for 2 h	50	[32]
2	25 μm Ti powder, 3.5 μm B_4C powder	Ball milling: 50 rpm, 24 h; Direct reaction synthesis method: 1073 K	59	[33]
3	$TiCl_4$, C_2Cl_6, Mg	Combustion synthesis (Ar gas): 865 °C, 10 min; Dried at 90 °C for 24 h	90	[34]
4	50 μm Ti powder, 0.1 μm Carbon black, 150 μm NaCl	Self-melting synthesis (Ar gas): 801.85 °C	20~100	[35]
5	$TiCl_4$, C_2Cl_4	Combustion synthesis method (Ar gas): 1173K	100	[36]
6	$TiCl_4$, C_2Cl_4, Mg	Magnesium thermal reduction method (with Ar gas): 850 °C	100	[37]
7	TiO_2, C	Magnesium thermal reduction: 800 °C, 4 h	50~100	[38]
8	TiO_2, CaC_2 (< 40 mm), $CaCl_2$	Carbon thermal reduction: 1000 °C, 2 h	50~100	[39]
9	24 nm Carbon black, 40 nm TiO_2,	Carbothermal reduction: 1549.85 °C, 4 h	100	[40]
10	TiO_2, Carbon black	Carbothermal reduction method (with Ar gas): 1550 °C, 4 h	300~600	[41]
11	Ti powder (< 20 μm), Graphite (< 10 μm)	Combustion synthesis method: 1100 °C (500 °C/min)	150±30~ 600±50	[23]
12	25 μm Ti powder, Carbon nanotubes	Low-speed ball mill: 50 r/min, 24 h. Pressed material heated by heater (30 °C/min) for 15 min.	490~1130	[42]
13	Titanic acid dimethyl ester ($Ti(OC_4H_9)_4$), Fructose ($C_6H_{12}O_6$), Acetylacetone (acac)	The precursor Ti-OC was prepared by the sol-gel method, and then it was carbonized by a carbonization process (in Ar): 1400 °C, 2 h	1000	[43]

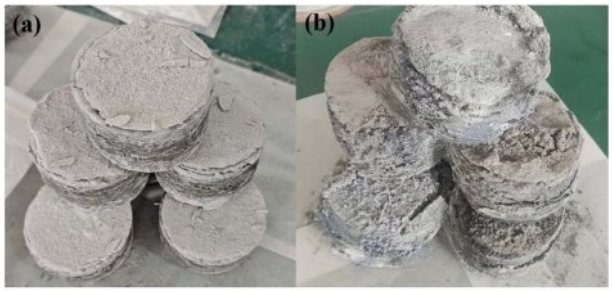

Fig. 12. Large-scale preparation of TiC powder: (a) before combustion, (b) after combustion.

at the micrometer scale; multi-step procedures (e.g., No. 1) significantly increase operational complexity; and the reliance on specialized raw materials (e.g., carbon nanotubes in No. 12) hinders scalability. In contrast, the salt-assisted combustion synthesis method employed in this study demonstrates considerable overall advantages in the synthesis of nanostructured TiC powder. First, the incorporation of NaCl effectively suppresses grain growth, yielding particle sizes substantially smaller than those achieved by most conventional methods (e.g., No. 7-10 and 13), which typically range from 100 to 1000 nm. Second, the method eliminates the need for additional post-treatment steps (e.g., drying in No. 1 and 3), and operates at a reaction temperature significantly lower than that of carbothermal reduction (>1400 °C) and molten salt synthesis (850 °C), thereby reducing energy consumption. Furthermore, the method utilizes low-cost and readily available micro-sized TiO_2 and carbon black as starting materials, thereby avoiding the challenges associated with the use of highly toxic $TiCl_4$ (No. 3, 5, 6), expensive carbon nanotubes (No. 12, 14), and technically demanding nanostructured precursors (No. 7-9). Most importantly, this study has achieved the successful scale-up production of high-melting-point TiC nanopowder (≥1 kg), with corresponding photographs of the production process provided in Fig. 12. The challenges of agglomeration control and thermal uniformity in large-scale processes can be effectively mitigated by increasing the number of reactors and raw material pressing piece. The reactor employs a crucible with a high aspect ratio to promote unidirectional propagation of the combustion wave. A stratified loading strategy is implemented by alternately filling the reactants and NaCl into the crucible, with porous ceramic spacers inserted between layers to further enhance uniform heat transfer.

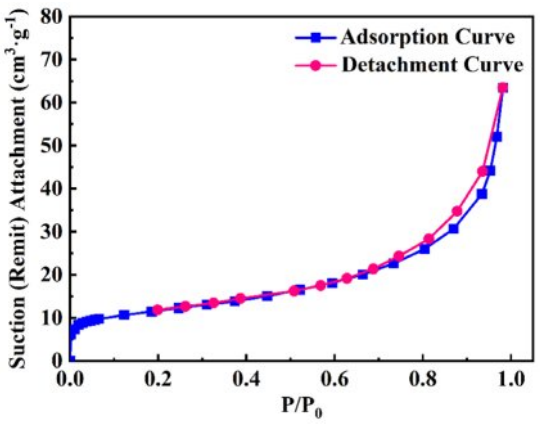

Fig. 13. The adsorption-desorption isotherm curve for synthesizing TiC with 100 wt.% NaCl.

Fig. 13 presents the adsorption-desorption isotherm of the TiC powder synthesized with the addition of 100 wt.% NaCl. The specific surface area of the TiC100 sample was determined using the static volumetric method, yielding a value of 15.203 m^2/g. Based on Eq. (2), the average particle size of individual TiC100 particles was calculated to be 80 nm. This result is in good agreement with the average particle size data presented in Table 3 and is further supported by the SEM and TEM analysis. The combustion synthesis method conducted in the NaCl molten salt medium enabled effective size control of the TiC nanoparticles, thereby achieving the successful and controlled synthesis of nano-sized TiC powder.

Formation mechanism of TiC nanopowder in diluent medium

In the TiO_2-C-Mg reaction system, all reactions occur within a sealed environment. Thermodynamic analysis reveals that during the combustion synthesis of TiC, the system's adiabatic temperature decreases from 3200 K to 1488 K. Compared to the reducing agent Mg powder, NaCl possesses a higher melting point, which facilitates the reduction process. During the preheating stage, as illustrated in Fig. 14a, nanoscale reactants are uniformly distributed among the auxiliary materials. When the system temperature exceeds 500 K, the ignition agent is activated, initiating a reaction that releases a significant amount of heat. As the temperature rises to approximately 1800 K, a self-propagating reaction is triggered among the reactants. Due to its lowest melting point, Mg begins to melt when the system reaches 923 K. The molten Mg infiltrates and diffuses into the solid particles, forming a coating layer, as shown in Fig. 14b. The reduction of oxides to form MgO is an exothermic reaction that generates a large quantity of heat in a short period. Upon reaching the melting point of NaCl (1076 K), the salt melts and absorbs heat, thereby reducing the rate of temperature increase and effectively suppressing rapid grain growth. Meanwhile, localized regions may reach the boiling point of Mg (1378 K), at which point Mg volatilizes into vapor, promoting a more complete reduction reaction, as depicted in Fig. 14c. When the system approaches the boiling point of NaCl (approximately 1700 K), the rate of temperature rise sharply declines due to extensive NaCl volatilization and associated heat absorption. The system reaches thermal equilibrium when the heat released by the magnesiothermic reaction equals the heat absorbed during NaCl phase transitions,

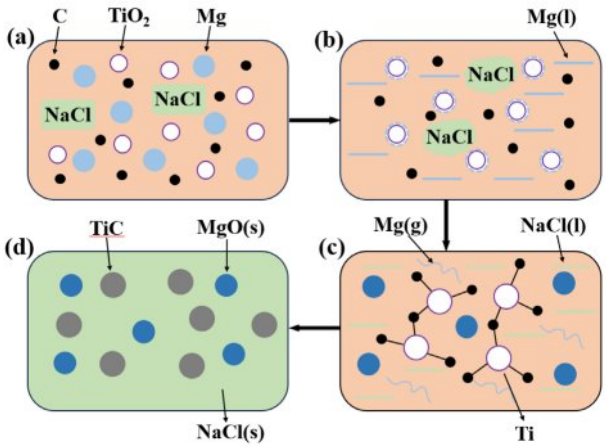

Fig. 14. The mechanism diagram of the role of the molten salt diluent in the TiO_2-C-Mg system: (a) initial state, (b) temperature-rise period, (c) constant temperature stage and (d) cooling stage.

at which point the temperature stabilizes at the adiabatic value. During the subsequent cooling phase, once the temperature drops below the melting point of NaCl, the molten salt solidifies and crystallizes, encapsulating the formed carbides and effectively preventing further particle growth, as shown in Fig. 14d.

During the combustion synthesis of nano-TiC powder, the molten salt diluent NaCl exerts a regulatory effect on both the formation and growth stages of the powder. In the carbide formation stage, the addition of low-melting-point NaCl facilitates the formation of a liquid-phase medium at relatively low temperatures, thereby enhancing the mobility of the reactants and significantly accelerating the diffusion rate. For instance, in the synthesis of TiC, this liquid-phase environment promotes effective contact between Ti and C, thereby facilitating the nucleation process. Furthermore, NaCl plays a crucial role during the particle growth stage. Excessively high temperatures or prolonged reaction times tend to promote grain growth, reduce powder activity, and lead to particle agglomeration. As the NaCl content in the system increases, the released reaction heat is absorbed, resulting in a decrease in the system's adiabatic temperature and a consequent reduction in crystal growth rate. Additionally, the introduction of molten salt enhances the degree of supercooling due to the increased cooling rate, which promotes a higher nucleation rate and enables the synthesis of finer carbide particles. Upon cooling and solidification of the molten NaCl, diffusion in the liquid-phase environment is suppressed, effectively preventing particle adhesion and facilitating the production of high-melting-point carbide powders with minimal agglomeration and uniform particle size. Moreover, as the NaCl content increases, the thickness of the protective molten salt layer on the carbide surface increases, further inhibiting grain growth. While regulating particle size, the molten salt diluent also significantly influences product purity. An increase in NaCl content reduces the system's thermal conductivity, leading to a higher level of free carbon on the powder surface. Concurrently, the reduced particle size and increased specific surface area enhance the surface oxidation tendency. Additionally, variations in the amount of NaCl added affect its volatilization during the reaction. When the NaCl content reaches 110 wt.%, volatilization is maximized, resulting in insufficient thermal energy to sustain the reduction reaction, which leads to incomplete reaction and a decrease in the final product's purity due to the presence of residual reactants and reducing agents.

Conclusion

In the TiO_2-C-Mg reaction system, the introduction of the molten salt diluent NaCl enabled the large-scale (>1 kg) synthesis of high-melting-point nano-TiC powder via the combustion synthesis method. Following acid washing and subsequent rinsing with distilled water, by-products such as MgO and NaCl were completely removed from the as-synthesized carbonized powder, yielding a single-phase TiC product. The purity of TiC in all samples exceeded 99 wt.%. With increasing NaCl content in the system, the particle size of TiC decreased, with the average particle size decreasing from 178 nm to 74 nm. The introduction of NaCl provided a liquid-phase environment that significantly enhanced the diffusion rate of reactants. Furthermore, during the cooling stage, the crystallization of molten salt helped suppress nanoparticle agglomeration. As the NaCl content increased, the phase transformation of the molten salt absorbed heat, leading to a decrease in the system's adiabatic temperature and an increase in the degree of supercooling. Consequently, the thickness of the molten salt layer formed on the carbide surface increased, effectively reducing the crystal growth rate and promoting nucleation. This ultimately resulted in further refinement of the nano-TiC particle size. This study provides technical guidance for the large-scale synthesis of nano-TiC powder and establishes a foundation for the application of TiC-based materials in high-end industries.

Acknowledgements

This work was supported by the Gansu Province Science and Technology Major Project (24ZD13GA018), the College Industry Support Plan of Gansu Province (2023CYZC-29), and the Tamarisk Outstanding Young Talents Program of Lanzhou University of Technology (062202).

References

1. J.-H. Lee and H.-K. Park, J. Ceram. Process. Res. 22[5] (2021) 590-596.
2. Y. Zhang, J. Sun, L. Guo, K. Fan, R. Riedel, and Q. Fu, J. Eur. Ceram. Soc. 42[1] (2022) 18-29.

3. W. Luo, H. Tang, R. Li, B. Liu, B. Hu, and Q. Zhen, J. Eur. Ceram. Soc. 45[14] (2025) 117530.
4. Y. Huang, Y. Zhang, Y. Lu, Y. Cheng, Y.h. Du, X. Zhou, and D. Liu, Ceram. Int. 51[26, Part B] (2025) 49307-49316.
5. L. Zhou, Y. Li, Z. Kou, L. Zheng, Q. Li, G. Ma, Y. Zhang, and D. He, J. Eur. Ceram. Soc. 44[8] (2024) 4887-4894.
6. S. Yu, J. Ceram. Process. Res. 24[3] (2023) 503-506.
7. R. Huang, and X. Yang, J. Ceram. Process. Res. 23[2] (2022) 213-220.
8. M. Abishaa, and J.P.A. Joseb, J. Ceram. Process. Res. 24[2] (2023) 242-249.
9. S.A. Rasaki, B. Zhang, K. Anbalgam, T. Thomas, and M. Yang, Prog. Solid State Chem. 50 (2018) 1-15.
10. T. Qin, Z. Wang, Y. Wang, F. Besenbacher, M. Otyepka, and M. Dong, Nano-Micro Lett. 13[1] (2021) 183.
11. H. Qiu, H. Wei, S. Ren, L. Sun, J. Li, Z. Wang, L. Zhao, C.-a. Wang, and Z. Xie, J. Ceram. Process. Res. 25[2] (2024) 212-219.
12. S.-H. Ko, J. Ceram. Process. Res. 13[S1] (2012) 105-109.
13. Q. Dong, J. Wang, M. Sun, S. Shen, T. Huang, Z. Yu, Z. Zhang, X. Wang, and S. Liu, Ceram. Int. 51[25, Part C] (2025) 46448-46459.
14. J. ur Rehman, Y. Zeng, S. Javed, O. Gohar, A. Ahmad, M. Bouyer, M. Mujahid, and M. Motola, Ceram. Int. 51[16, Part A] (2025) 21590-21599.
15. A. Rajabi and M.J. Ghazali, Ceram. Int. 43[16] (2017) 14233-14243.
16. A.A. Gaber, H.K. Abd El-Hamid, R.E.A. Ngida, H.E.H. Sadek, and R.M. Khattab, Ceram. Int. 50[20, Part B] (2024) 38917-38932.
17. J. Hu, H. Peng, C. Hu, W. Guo, X. Tian, and Y. Peng, J. Ceram. Process. Res. 18[1] (2017) 79-85.
18. H. Jia, Z. Zhang, Z. Qi, G. Liu, and X. Bian, J. Alloys Compd. 472[1-2] (2009) 97-103.
19. A. Fahmi and F. Amin, New Math. Nat. Comput. 15[01] (2019) 145-167.
20. L. Wang, Z. Yang, and J. Li, J. Am. Ceram. Soc. 106[7] (2023) 4023-4027.
21. G. Saito, K. Harada, and Y. Kagami, J. Am. Ceram. Soc. 108[9] (2025) e20672.
22. Q. Meng, G. He, Z. Yang, and J. Li, J. Am. Ceram. Soc. 107[12] (2024) 7966-7972.
23. H. Ghazanfari, C. Blais, H. Alamdari, M. Gariépy, S. Savoie, and R. Schulz, Surf. Coat. Technol. 360 (2019) 29-38.
24. G. Zhu, W. Wang, R. Wang, C. Zhao, W. Pan, H. Huang, D. Du, D. Wang, D. Shu, and A. Dong, Materials 10[9] (2017) 1007.
25. F. Zhan, R. Bai, X. Liu, K. Xu, H. Zhang, M. Zhu, Y. Zheng, S. Xu, J. Sheng, and P. La, J. Ceram. Process. Res. 25[4] (2024) 490-498.
26. R. Bai, F. Zhan, H. Zhang, M. Zhu, Y. Zheng, and P. La, J. Ceram. Process. Res. 26[2] (2025) 219-230.
27. S. Zeng, M. Xiao, X. Liu, Y. Wu, K. Li, Z. Qiu, and D. Zeng, Mater. Res. Express 6[12] (2020) 1265h5.
28. H. Yin, X. He, G. Song, Y. Yu, Y. Zheng, and Y. Bai, Mater. Sci. (2022).
29. C.L. Yaws, Elsevier 4 (2013).
30. O. Coban, M. Bugdayci, and M.E. Acma, J. Aust. Ceram. Soc 58[3] (2022) 777-791.
31. Y.F. Wang, Z.M. Fan, and F. Zhu, Solid State Phenom. 331 (2022) 203-207.
32. L. Yang, Y. Wang, R. Liu, H. Liu, X. Zhang, C. Zeng, and C. Fu, J. Mater. Sci. Technol. 37 (2020) 173-180.
33. X.-D. Ma, H.-Y. Yang, B.-X. Dong, S.-L. Shu, Z. Wang, Y. Shao, Q.-C. Jiang, and F. Qiu, Mater. Sci. Eng. A 869 (2023) 144810.
34. S. Dyjak, M. Norek, M. Polański, S. Cudziło, and J. Bystrzycki, Int. J. Refract. Met. Hard Mater. 38 (2013) 87-91.
35. H. Nersisyan, J. Lee, and C. Won, J. Mater. Res. 17[11] (2002) 2859-2864.
36. D.-W. Lee, J.-H. Yu, J.-Y. Yun, F.R. Turaev, T.-H. Lim, and A.T. Jang, J. Ceram. Process. Res. 9[4] (2008) 407-410.
37. D.W. Lee, Y.K. Baek, I.S. Seo, J.N. Kim, and J.P. Wang, J. Nano Res. 23 (2013) 1-6.
38. T. Niu, B. Zhou, Z. Zhang, X. Ji, J. Yang, Y. Xie, H. Wang, and A. Du, Nanomaterials 10[12] (2020) 2527.
39. Z. Jiang, N. Kong, H. Xu, Y. Wei, and B. Li, J. Alloys Compd. 1010 (2025) 177410.
40. K.-H. Wu, Y. Jiang, S. Jiao, K.-C. Chou, and G.-H. Zhang, J. Mater. Res. Technol. 9[5] (2020) 11778-11790.
41. R. Koc, J. Mater. Sci. 33 (1998) 1049-1055.
42. J. Liu, Y.-L. Li, A.-M. Li, H.-Y. Yang, B.-X. Dong, X.-M. Zhong, C.-G. Wang, Z.-G. Li, D.-L. Chen, Y. Yu, S.-L. Shu, C.-J. Luo, J. Qiao, M. Zhu, F. Qiu, and Q.-C. Jiang, Ceram. Int. 51[4] (2025) 4400-4411.
43. L. Gao, Y. Zhang, X. Yang, Y. He, and L. Song, J. Ceram. Process. Res. 21[6] (2020) 615-621.